



A closed-host bi-layer dense/porous solid electrolyte interphase for enhanced lithium-metal anode stability

Corey M. Efaw^{1,2}, Bingyu Lu³, Yuxiao Lin¹, Gorakh M. Pawar¹, Parameswara R. Chinnam¹, Michael F. Hurley², Eric J. Dufek¹, Ying Shirley Meng³, Bin Li^{1,*}

¹ Energy and Environmental Science and Technology, Idaho National Laboratory, Idaho Falls, ID 83415, USA

² Micron School of Materials Science and Engineering, Boise State University, Boise, ID 83725, USA

³ Department of NanoEngineering, University of California San Diego, La Jolla, CA 92093, USA

Thanks to its high specific capacity and low electrochemical potential, lithium metal is an ideal anode for next-generation high-energy batteries. However, the unstable heterogeneous surface of lithium gives rise to safety and efficiency concerns that prevent it from being utilized in practical applications. In this work, the formation of a closed-host bi-layer solid electrolyte interphase (SEI) improves the stability of lithium metal anode. This is successfully realized by forming an interconnected porous LiF-rich artificial SEI in contact with Li metal, and a dense, stable in-situ formed upper layer SEI. The porous layer increases the number of Li/LiF interfaces, which reduces local volume fluctuations and improves Li⁺ diffusion along these interfaces. Additionally, the tortuous porous structure guides uniform Li⁺ flux distribution and mechanically suppresses dendrite propagation. The dense upper layer of the SEI accomplishes a closed-host design, preventing continuous consumption of active materials. The duality of a dense top layer with porous bottom layer led to extended cycle life and improved rate performance, evidenced with symmetric cell testing, as well as full cell testing paired with sulfur and LiFePO₄ (LFP) cathodes. This work is a good example of a rational design of the SEI, based on comprehensive consideration of various critical factors to improve Li-metal anode stability, and highlights a new pathway to improve cycling and rate performances of Li metal batteries.

Keywords: Li-metal batteries; Artificial solid-electrolyte interphase; Closed-host design

Introduction

The drastic costs of global warming, both environmentally and economically, are driving the necessity to diminish a dependency on oil and gas for energy applications. Alternative clean energy reliance has been at the forefront of global investment for a more sustainable future. Part of this transitional effort is focused on energy storage via a rechargeable battery. Lithium metal is often considered the “Holy Grail” of rechargeable

battery technology, due to its high theoretical capacity (3,860 mAh/g) and low electrochemical potential (−3.04 V vs. SHE), which has the practical capability of achieving a specific energy above 500 Wh/kg when paired with a high-theoretical capacity sulfur or high-voltage Ni-rich LiNi_{1-y-z}Mn_yCo_zO₂ (NMC) cathode [1–8].

However, there are key issues that limit the commercialization of rechargeable Li-metal batteries (LMBs), including poor cycling performance or safety concerns from short circuiting. The poor performance of lithium metal arises from its unavoidably

* Corresponding author.

E-mail address: Li, B. (bin.li@inl.gov)

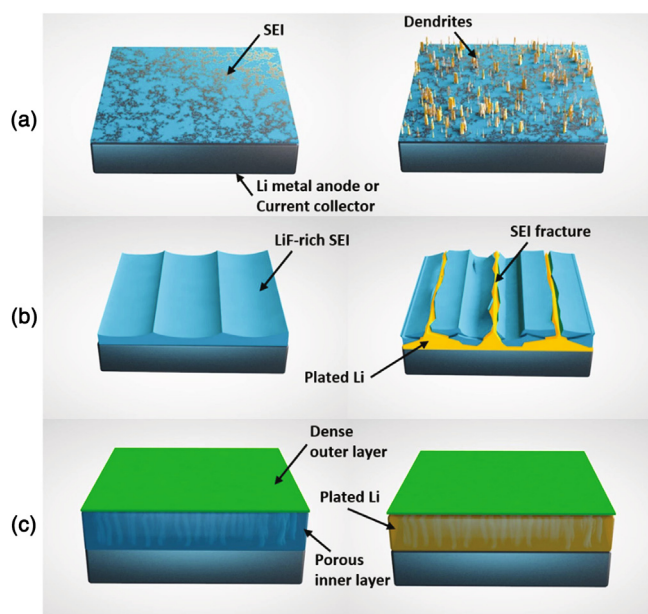


FIGURE 1

Schematic showing the initial structure and failure mechanism for (a) Li-metal and (b) dense LiF artificial SEI, as well as (c) the plating mechanism for a bi-layer dense/porous artificial SEI.

heterogeneous surface (Fig. 1a). The innate variability in mechanical and electrochemical properties of lithium's native film of oxides and carbonates initiates a cascading effect of heterogeneity into the solid-electrolyte interphase (SEI), ending with an uneven electric field and Li^+ flux distribution [9]. The susceptibility of increased Li^+ flux at thermodynamically favorable sites (e.g., dislocations, grain boundaries, crystallographic and topographic heterogeneities, etc.) caused by phenomena such as the "tip effect" [10,11] leads to dendrite formation, causing rapid failure via short circuiting. Meanwhile, dendrites with high specific surface area spontaneously react with the electrolyte, rendering accumulation of resistive SEI and formation of isolated lithium (i.e., "dead Li") during lithium stripping, thereby driving continuous loss of active material (LAM) at the anode side as well as increased cell impedance [6,7,12]. To minimize dendrite growth and LAM, a robust and stable SEI that permits uniform Li^+ flux must be formed on the Li-metal anode.

The ideal SEI should be dense, mechanically and electrochemically stable to hinder side reactions, electronically insulating to prevent lithium deposition on the SEI, ionically conductive to improve diffusion kinetics, and homogeneous to support uniform Li^+ flux and suppress dendrite growth [12–16]. The spontaneously formed traditional organic–inorganic mixed SEI has poor mechanical strength and loosely formed structure, and thus struggles to tolerate the big volume variation of the electrode during (dis)charging [16,17]. The inability to control the specific components of the in-situ formed SEI could cause non-uniform Li^+ flux and ramify deposition, as well as continuously consume active materials, leading to poor reversibility and shortened cycle life.

Rational design of the electrolyte is of great importance to obtain a high-performance SEI. For example, it was observed that

the addition of fluoroethylene carbonate (FEC) to a carbonate-based solvent shifted the SEI from a mosaic (i.e., mixed amorphous and crystalline) to a multilayered (i.e., layered amorphous and crystalline) structure. The variability in crystalline grain distribution has a severe impact on ionic flux distribution [16]. Others have shown that additives such as LiNO_3 improve the cyclability of Li||S batteries by forming a stabilized SEI, in addition to lessening the polysulfide shuttling effect [3,4,18,19]. An electrolyte with salt aggregation and limited solvation to Li^+ , such as high-concentration electrolytes (HCE) and localized high-concentration electrolytes (LHCE), can increase the salt's reduction potential and render a salt-reduced SEI layer (e.g., inorganic LiF-rich) rather than a solvent-reduced SEI layer (e.g., mixed organic–inorganic) [20–23]. Such salt-driven inorganic SEI, in general, has a lower affinity to Li metal than a solvent-driven SEI, and thus can withstand structural damage over repeated volume fluctuations during the cell's lifetime.

Comparing with the in-situ formed SEI via electrolyte optimization, the composition and structure of a pre-treated artificial SEI on lithium is more controllable. An inorganic SEI (e.g., LiF) is promising due to its wide electrochemical stability window, low solubility, and low adhesion to Li metal [24–27]. However, a traditional dense inorganic SEI is generally brittle, and cracks appear over cycling due to the non-uniform lithium deposition caused by an unavoidably heterogeneous or non-conformal SEI (Fig. 1b) [25,26]. Hence, new methodologies to form a reliable SEI is highly desirable. For example, Mai and co-workers proposed a lithiophilic/lithiophobic gradient interfacial layer design, which can realize gradient Li^+ distribution to increase Li^+ concentration far from the separator side, thus decreasing the risk of short circuit. An underlying lithiophilic ZnO/carbon nanotubes (CNTs) layer stabilized the SEI and simultaneously inhibited dendrite growth, while the upper lithiophobic CNTs layer with a high modulus suppressed mossy dendrites from piercing the separator [28]. Xie and co-workers found that controlling the electric field distribution can help to localize Li^+ flux. Coating the side of the separator facing the lithium anode with an electron-conducting functionalized nanocarbon or ultrathin copper film could regulate bidirectional dendrite growth on both separator and anode to avoid short circuit [29]. In addition, the design of hosting lithium inside a mixed ion and electron conductive scaffold or matrix has been extensively utilized [10,30,31]. The high specific surface area of the 3-D scaffold decreases the local current density and thus minimizes dendrite formation, based on Sand's formula in the "Space Charge Model" [32,33]. The resultant host provides confined space to accommodate Li plating/stripping, thus lessening electrode volume changes. However, for the designs mentioned above, lithium is still exposed directly to the electrolyte, and thus parasitic reaction cannot be easily mitigated [33]. Therefore, a closed host is critically important for stabilizing the Li-metal anode.

Accordingly, we propose a closed-host bi-layer SEI structure on lithium metal (Fig. 1c). The following are our design principles for such an SEI structure. The outer SEI layer should be ionically conductive and relatively dense to mitigate consumption of active materials. Beneath the dense layer, an inorganic-rich and porous structure in contact with lithium metal can help mechanically inhibit SEI fracture, guide Li^+ flux and ensure

uniform Li plating/stripping. The porous SEI must at least be ionically conductive and the pores should be interconnected. In this case, the lithium can only be plated at the Li/SEI or current collector/SEI interface, while the electron involved in the redox reaction transports through deposited Li metal. The material of the porous structure should be lithiophobic with high interfacial energy against Li to maintain a stable porous structure over cycling. If the porous material also exhibits electronic conduction, the interconnectivity is not necessary, and lithium is able to nucleate at the available pore sites in the frame structure. In this work, we demonstrated such a bi-layer SEI structure, consisting of an interconnected, porous LiF-rich artificial SEI and a dense inorganic-rich in-situ formed SEI, which was verified to improve cycling performance.

Material and methods

Materials synthesis

Lithium foil (170 μm , MTI Corporation) is punched into ~ 1.43 cm diameter disks and rolled onto spacers. The samples are then gently polished at two perpendicular directions for 5 s each way to remove native film. A mixed SEI film of LiI and LiF is produced from reaction between polished lithium and a precursor solution. The precursor solution was made by adding 50 mg of polyvinylidene fluoride (PVDF, Sigma-Aldrich, MW $\sim 534,000$) and 66 mg of iodine (Fisher Scientific) to 10 mL N, N-dimethylformamide (DMF, Sigma-Aldrich). Elementally, this describes the 1:3 I:F ratio solution; varying the amount of iodine in the precursor produces different I:F ratios (22 mg for 1:9 I:F, 40 mg for 1:5 I:F, and 198 mg for 1:1 I:F). Similar deposition of a dense LiF artificial SEI is done by excluding iodine in the precursor solution [14]. The artificial SEI is deposited by placing a ~ 1.59 cm diameter Celgard[®] 2325 separator wetted with the precursor solution onto the polished lithium foil for 3–5 s [14]. Removal of LiI from the artificial SEI and formation of the porous LiF SEI is done by rinsing the surface with equal parts 1,3-dioxolane (DOL, Sigma-Aldrich) and dimethoxyethane (DME, Sigma-Aldrich) solvent, followed by drying in a glovebox.

Cathode preparation

The sulfur cathode was produced by mixing 1.28 g sulfur (Fisher Scientific, 99.5%) with 0.52 g super P (EQ-Lib-SuperP, MTI Corporation) conductive agent. This mixture was ball milled and further heat treated at 155 $^{\circ}\text{C}$ in an autoclave. 0.2 g PVDF binder mixed in 1-methyl-2-pyrrolidone (NMP, Sigma-Aldrich, $\geq 99\%$) solution is added to the S-C mix with an additional 5 g of NMP solvent, mixed with three 5 mm diameter zirconia balls in an ARE-310 Thinky Mixer for 5 min, resulting in 64% active mass. The slurry was rolled onto a 20 μm carbon-coated Al current collector (MTI Corporation) and dried in a furnace with dry air flow at 80 $^{\circ}\text{C}$ for three days. The resultant electrode has 3 mg/cm^2 of active sulfur weight with a porosity of 80–90%. The practical specific capacity for 1C of this sulfur cathode is defined as 1000 mAh/g (i.e., 3 mAh/cm^2). LiFePO₄ (LFP) cathode was purchased from BASF. An active mass of 85 wt.% is confirmed, with inclusion of 7.5% PVDF binder and 7.5% carbon black. Practical specific capacity of LFP is defined as 2.4 mAh/cm^2 , with a mass loading of 13.97 mg/cm^2 (~ 172 mA/g). Both cathodes were

punched into 1.27 cm diameter disks and dried in vacuum prior to loading into glovebox for cell construction.

Electrochemical measurements

Galvanostatic cycling of symmetric coin cells was done with a MACCOR Model 2200 (Maccor, Inc.). 32 μL of 1 M lithium bis(trifluoromethanesulfonyl)imide (LiTFSI, BASF) and 2 wt.% of lithium nitrate (LiNO₃, Sigma-Aldrich) mixed in 1:1 DOL:DME was used as the electrolyte in each symmetric cell. LiNO₃ was also excluded from symmetric cells to observe the effect of the additive on the formation of the bi-layer SEI structure.

Galvanostatic cycling of Li||S was done between 1.8 and 2.6 V operating at a C/5 rate following two C/20 formation cycles, with an electrolyte to sulfur ratio of 10 $\mu\text{L}/\text{mg}$. For Li||LFP, cycling was done between 2.5 and 4.2 V operating at C/2 rate following three C/5 formation cycles, with 36 μL electrolyte per cell. Rate performance testing (RPT) of both systems was done at different C-rates (5 cycles per rate), examining cycle durability with a final 10 cycles at C/2 rate. Electrochemical impedance spectroscopy (EIS) was used to analyze impedance spectra for symmetric cells. 10 μA perturbation was used to acquire impedance spectra within a range of 1 MHz–0.1 Hz. At least 4 coins cells for each condition were repeated. Majority showed similar performance.

Characterization

Different characterization techniques were utilized both after treatments and after cycling. Post-mortem samples were disassembled in a glovebox, rinsed with 1:1 DOL:DME, and dried in vacuum prior to analysis. A PHI-5600 XPS (Physical Electronics) with an Al (K α) source was used to provide surface analysis, along with an Ar⁺ ion gun (2 kV, 1.2 μA) for sputter depth profiling. A FEI Teneo FESEM was used to observe morphology and elemental make-up (via energy dispersive X-ray spectroscopy, EDS). FEI Scios DualBeam FIB-SEM system was used to conduct the cryo-FIB-SEM characterization. All samples were transferred from glovebox to the FIB-SEM chamber with an air-tight transfer holder to minimize air exposure. The sample was cooled to -180 $^{\circ}\text{C}$ with liquid nitrogen using the built-in cooling pipeline to minimize the beam damage to the sample. Gallium ion beam with a voltage of 30 kV, current of 7 nA and dwell time of 100 ns was used to roughly mill down the cross-section of the deposited lithium followed by a cleaning process with ion beam at 1 nA. The SEM images of the cross-section were taken using Everhart-Thornley Detector (ETD) at 5 kV and 0.1 nA. Atomic force microscopy (AFM) techniques were used to acquire maps of nanoscale properties of polished Li. Quantitative nanomechanical mapping (QNM) was used to quantify mechanical properties such as adhesion, modulus, and deformation, calibrated with a nominally 8-nm Sb-doped Si probe (Bruker Corporation). Scanning Kelvin probe force microscopy (SKPFM) provided simultaneous maps of surface topography and electronic properties (i.e., Volta potential difference). This is employed in a dual pass, frequency modulated (FM), PeakForce (PF, Bruker Corporation) method to acquire spatially resolved Volta potentials, operating in a pseudo capacitor-like method at a constant lift height of 100 nm above the surface. A nominally 5-nm, Si-based probe with an Al-coated cantilever (Bruker Corporation) was used for SKPFM acquisition, calibrated with a relatively inert gold standard for

repeatable results [34]. Both techniques were done on a Bruker Dimension Icon AFM equipped with a 64-bit NanoScope V controller, inside an inert glovebox (MBraun, <0.1 ppm O₂ and H₂O).

Computational details

Large-scale Atomic/Molecular Massively Parallel Simulator (LAMMPS) [35] code was used to perform all molecular dynamics (MD) simulations. Ovito tool was used to perform all atomic trajectory visualization [36]. Further specifics to each simulation are provided below.

The role of DMF to form LiF-rich SEI

The PVDF molecule solvation/de-solvation processes in DMF and N,N-dimethylacetamide (DMA) solvents were investigated, ensued by the examination of the PVDF migration and stabilization near the Li-DMF and Li-DMA interfaces. A stabilized PVDF near the Li-solvent interface could be beneficial in enhancing Li-PVDF electrochemical interaction, and a formation of the LiF artificial structure.

The initial Li/DMF/PVDF and Li/DMA/PVDF molecular geometry constructions, and the subsequent pcff+ forcefield assignment were performed in the Medea simulation environment [37]. The pcff+ force field, which comprised of the bond, angle, dihedral, improper, Coulombs, and Lennard-Jones (LJ) 6–9 interactions, was used to model the Li/DMF/PVDF and Li/DMA/PVDF atomic interactions. The pppm algorithm was used to calculate the long-range Coulombic interactions. Lithium-metal was treated as rigid without any atomic charges. A more refined and sophisticated forcefield (e.g., MEAM [38] or ReaxFF [39]) can be used to obtain a refined simulation result. A canonical (NVT) ensemble with a periodic boundary condition was used with a timestep of 0.1 fs, total simulation time of 1 ns, and frequency of saving the atomic trajectory information every 1 picosecond (ps).

The stability of LiF and Lil interface

Embedded ion method (EIM) [40] was used to validate the accuracy of the EIM potential to model LiF and Lil phases. Subsequently, a combined Lil-LiF system was investigated in an isobaric-isothermal (NPT) ensemble with periodic conditions at 1 atm and 300 K, with a timestep of 1 fs for a 25 ps length of simulation for individual LiF and Lil phases and 500 ps for the combined Lil-LiF interface with atomic trajectory information collected every 1 ps.

Li⁺ transport energy barriers

Li-Li interaction in any Li crystal was described by the MEAM force field.[38] The Li-Li, F-F, and Li-F interaction in a LiF crystal, as well as between Li and LiF crystals were all described in a universal force field [41]. Energy barriers of Li⁺ transport through bulk LiF, along LiF surface, and between a Li-LiF interface were observed. LiF(001) and Li(001) have the lowest surface energy [42], and thus were chosen to build the Li-LiF interface. A 7 × 7 × 7 Li supercell and 6 × 6 × 6 LiF supercell were combined to construct the Li(001)-LiF(001) interface, giving only 0.2% mismatch in the lattice parameters. For comparison, a 6 × 6 × 12 LiF supercell was produced in an individual simula-

tion. The charge of Li⁺ and F⁻ in LiF were set to ±0.8, according to previous research [43].

Stress-strain testing

The as built LiF and Li-LiF simulation cells were first ran in an NPT ensemble for 500 ps for equilibration. The equilibrated density of LiF is 2.52 g/cm³, which is close to experimental data. After that, the equilibrated structures were put into a tensile testing simulation. Stretch strain was performed under a constant strain rate of 0.05 ps⁻¹ until strain reached 20%. The compression strain of the other two directions were applied according to a Poisson's ratio of 0.326 [44].

Results and discussion

A proof-of-concept closed-host bi-layer dense/porous SEI on Li-metal anode surface was demonstrated in this work. LiF was selected for the porous frame structure, due to its wide electrochemical stability window against Li, low solubility in electrolytes, and superior mechanical properties [14,15,19,24–27]. In addition, LiF has a high interfacial energy against Li (i.e., lithiophobic), which can suppress dendrite nucleation and growth inside LiF, based on the Butler-Volmer model [7,25,45]. Nevertheless, the biggest issue for LiF as SEI is its low ionic conductivity, but Li ion transport along Li/LiF interfaces can be greatly enhanced, which will be discussed later. As mentioned in the introduction, the LiF-rich pores should be interconnected, as LiF is electronically insulating. Here, through a simple method of producing a mixed Li-LiF surface composite by reaction of polished lithium metal with a precursor solution of polyvinylidene fluoride (PVDF) and iodine (I₂) dissolved in N,N-dimethylformamide (DMF) [14], followed by a solvent rinse (equal parts 1,3-dioxolane, DOL and dimethoxyethane, DME) to dissolve the Lil, a porous LiF-rich artificial SEI structure is produced. Comparing with dimethylacetamide (DMA), DMF as the precursor solvent was found to promote the reaction between PVDF and Li-metal, since a stabilized PVDF near the Li-solvent interface could be beneficial in an enhancement of the Li-PVDF electrochemical interaction and stabilization of the artificial LiF SEI structure. The DMF solvent is vital for promoting the initial reaction, as evidenced by a molecular dynamics (MD) simulation where PVDF mobility in DMF is superior when compared to PVDF in DMA (See details in Fig. S1).

Fig. 2a–d presents the surface and cross-sectional morphology, as well as X-ray photoelectron spectroscopy (XPS) of the resultant Lil-LiF composite. As is displayed in XPS results, LiF and Lil are successfully formed. These peaks remain as a function of depth, suggesting relatively uniform distribution throughout the ~4 μm thick composite, although a small number of pores were still observed in its cross-section, due to slight dissolution of formed Lil in the DMF solvent. Seen with EDS mapping, there is an intermingling of iodine and fluorine (Fig. S2f). According to MD simulation, intermixing of Lil and LiF does not occur, confirming Lil-LiF interfaces present within the composite (Fig. S3e). Lil phase easily dissolves into DOL:DME solvent, leaving behind a porous LiF-rich artificial SEI structure (Fig. 2e–h). XPS depth profiling confirms the absence of Lil after rinsing, while LiF is retained throughout the artificial SEI. The absence of Lil along the depth direction implies that interconnected

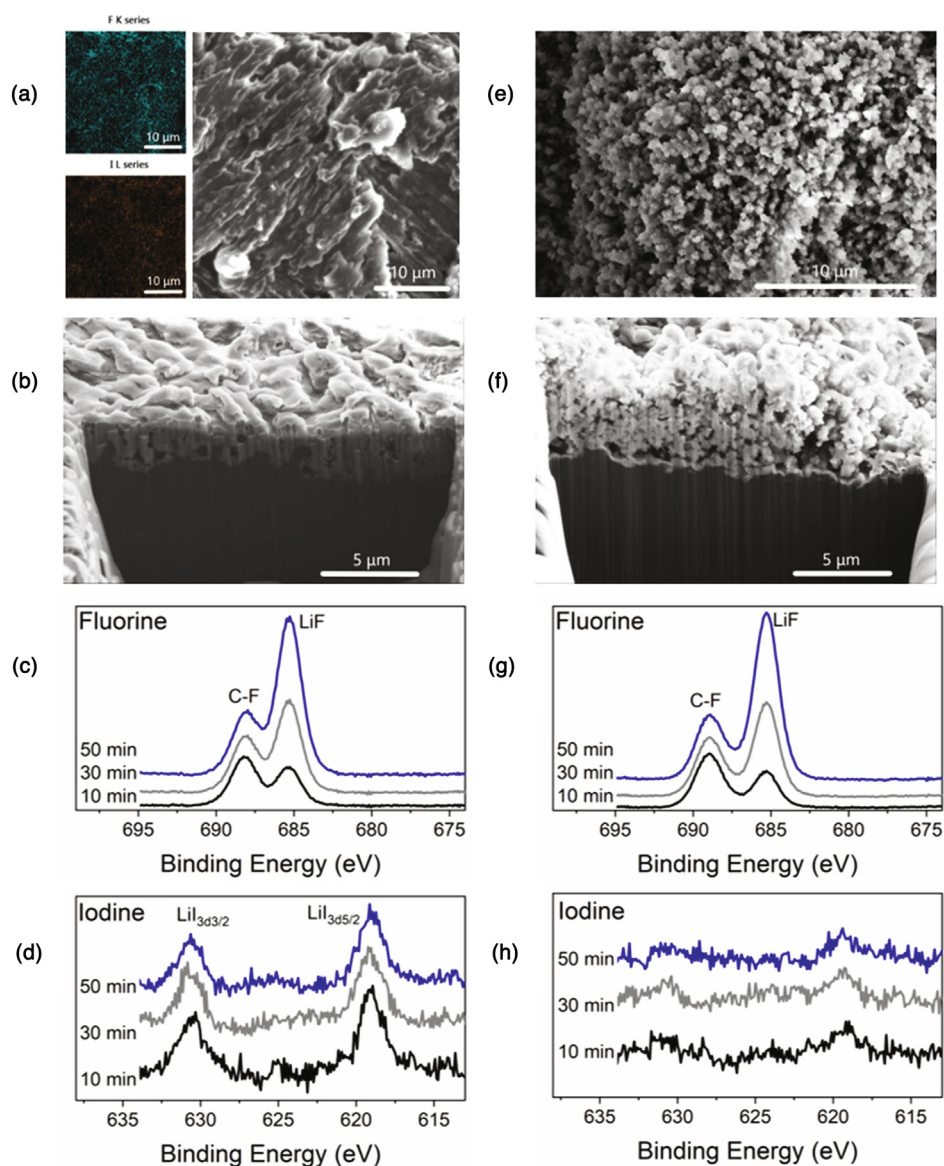


FIGURE 2

(a) FESEM and EDS, (b) cross-sectional cryo-FIB-SEM, (c) fluorine and (d) iodine XPS depth profile of the mixed LiI-LiF composite film. (e) Surface and (f) cross-sectional cryo-FIB-SEM, (g) fluorine and (h) iodine XPS depth profile of the porous LiF artificial SEI after rinse with DOL:DME.

pores are constructed, which is a must for an electronically insulating LiF-rich structure. The interconnectedness of the SEI allows Li plating and stripping in the pores and electronic transportation through the plated Li. The resultant porous artificial SEI is $\sim 4\text{--}5\ \mu\text{m}$ thick with an interconnected network of pores varying in size, ranging 100s of nanometers. For comparison, exclusion of I_2 in the precursor solution results in formation of a denser LiF-rich SEI layer with a thickness of less than $1\ \mu\text{m}$ (Figs. S2b and S4). The dissolution of LiI from DMF during the initial reaction led to available Li sites for further reaction, resulting in subsequently thicker LiI-LiF composite layer or porous LiF artificial SEI.

The open-frame porous structure is not designed to restrict parasitic side reactions between lithium and the electrolyte, therefore a relatively dense SEI layer should be formed either ex-situ or in-situ on top of the porous structure to realize the

design of a closed host (Fig. 3a). The top dense SEI layer prefers to be in-situ formed; otherwise, the bottom porous structure would be easily destroyed (e.g. pores being filled) by ex-situ process, such as physical vapor deposition, chemical vapor deposition and so on. In this work, the approach of an in-situ SEI was adopted by reaction with an additive in the electrolyte, such as FEC in carbonate-based solvents [46–50] or LiNO_3 in ether-based solvents [3,18,19]. Additives such as these have shown to form a passive inorganic-rich SEI layer to protect the Li-metal anode. Further, the material of open-frame porous structure prefers to be electrically insulating (e.g. LiF-rich) rather than traditional mixed ion and electron conductive (e.g. carbon-based). Otherwise, lithium will nucleate at the available pore sites in the mixed-conductive frame structure and SEI will be in-situ formed anywhere within the pores, rather than only on the top of porous structure. Since optimizing electrolyte additives is

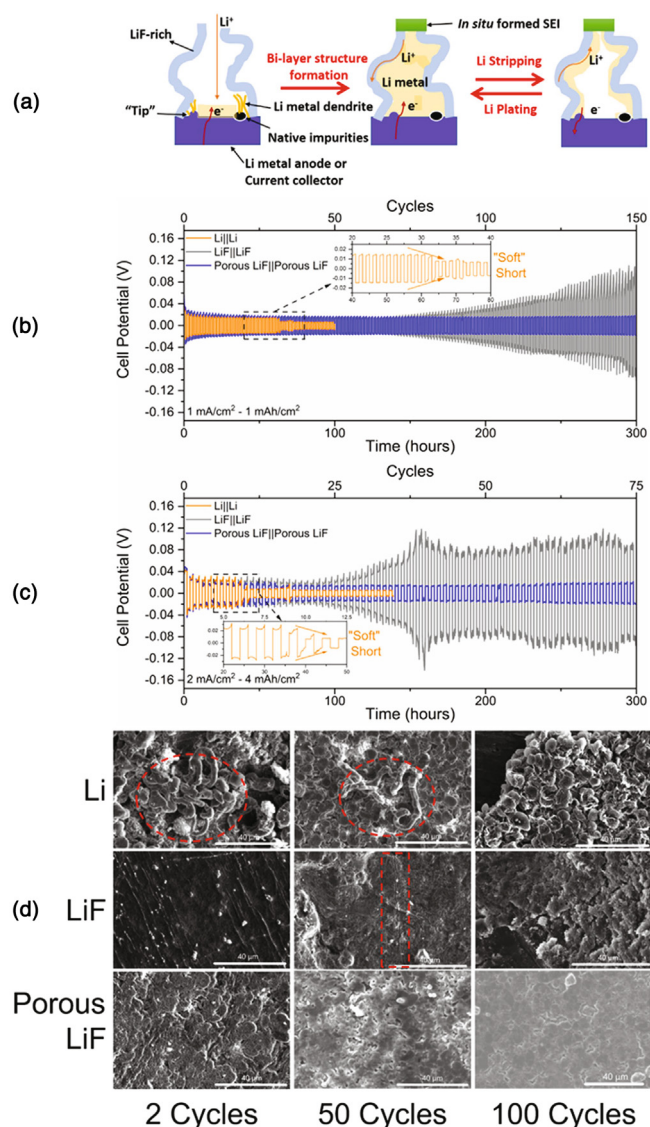


FIGURE 3

(a) Schematic showing the development and retention of the bi-layer SEI structure. (b and c) Symmetric cell cycling of different anode treatments at (b) low (1 mA/cm², 1 mAh/cm²) and (c) high (2 mA/cm², 4 mAh/cm²) current density and areal capacity, with (d) post-mortem FESEM of 1 mAh/cm² lithiated electrodes at increasing cycles.

not the focus of this work, 2 wt.% LiNO₃ was used in addition to 1 M lithium bis(trifluoromethanesulfonyl)imide (LiTFSI) in a 1:1 DOL:DME ether-based electrolyte as an example to demonstrate the closed-host bi-layer design.

The electrochemical testing of symmetric cells, assembled as Li||Li, LiF||LiF and porous LiF||porous LiF was conducted with different current densities and areal capacities (Fig. 3b and c and Fig. S5). Fig. 3d shows the corresponding evolution of different anode surface morphologies over cycling, which were characterized with Field Emission-Scanning Electron Microscope (FESEM). The presence of chemical and topographic heterogeneities (Figs. S2a, S6 and S7) drives the growth of dendrites on polished lithium metal (Fig. 3d). Correspondingly, evidence of dendrite growth is clearly seen in the symmetric cell voltage profile as a “soft” short circuit (after 31 and 9 cycles, respectively to Fig. 3b

and c), where an aggregate of lithium dendrites press into the separator but don't penetrate to make contact with the opposite electrode [51]. This is also evident at higher current densities (Fig. S5).

When a dense LiF-rich artificial SEI is formed on the polished lithium, susceptibility to dendrite growth is reduced, if not completely removed. Rather, the failure mechanism shifts to continuous Li loss. Evidenced with post-mortem FESEM analysis, the surface morphology shifts from granular for polished lithium to a single component-like structure for LiF in the early cycles, suggesting lithium growth under the insulating SEI layer and early stability (Fig. 3d). As cycling continues, the large volume fluctuations during Li plating/stripping and non-uniform Li⁺ flux leads to high local stress and fracture of the dense LiF-based SEI, surfacing fresh sites for new SEI to form via consumption of lithium and electrolyte. Over time, this consumption leads to a more resistant ionic pathway, resulting in the increased overpotential as cycling progresses (Fig. 3b–c and Fig. S5). With the chemical treatment described here, as well as by others [14], the retention of native species can still be present (Fig. S2c), causing non-uniform Li⁺ flux and susceptibility to SEI fracture. The removal of native species in the interphase and formation of a conformal SEI is very challenging to accomplish.

However, a porous SEI structure directly in contact with lithium can minimize the influence of native species. As shown in Fig. 3d, the post-mortem analysis reveals a relatively uniform surface without dendrites or cracking over extended cycles. A dense, uniform SEI is present as a bi-layer, where an in-situ SEI forms over the top of the porous artificial SEI, stabilizing the closed-host design and drastically reducing active consumption of underlying lithium. That agrees well with much improved symmetric cell cyclability, as minimal voltage hysteresis is maintained when compared to the dense LiF artificial SEI (Fig. 3b–c and Fig. S5).

The underlying mechanisms resulting in the longer lifespan based on a bi-layer SEI structure was deeply investigated (Fig. 3a). The dendritic growth driven by the presence of chemical or topographical heterogeneities can be suppressed in a process of lithium metal percolating through the tortuous and interconnected pores. The pore walls will not be penetrated or damaged, retaining the interconnected porous structure, due to high interfacial energy between LiF and Li [27,52]. As metallic lithium grows through the pores during the plating process, the exposed upper region of the plated Li metal in the porous structure is consumed via reaction with electrolyte, forming a relatively dense, inorganic-rich protective SEI layer, drastically reducing continuous reaction between Li and electrolyte. The top SEI layer has no native species and is relatively homogeneous, which would benefit uniform Li⁺ flux. As cycling continues, the pathway for fast Li⁺ transport is through the interconnected LiF|Li interfaces (Fig. 3a), as evidenced with MD simulations (Fig. 4a and b). Here, the LiF|Li interface has a drastically lower energy barrier for Li⁺ transport (0.60 eV) when compared to ionic transport through bulk LiF (1.30 eV) and along LiF surface (1.23 eV). Therefore, the increased thickness of the porous LiF layer (Fig. 2f) compared to the dense LiF layer (Fig. S4b) should not cause a drastic increase in impedance, as LiF|Li interface is more ionically conductive, which agrees well with rate

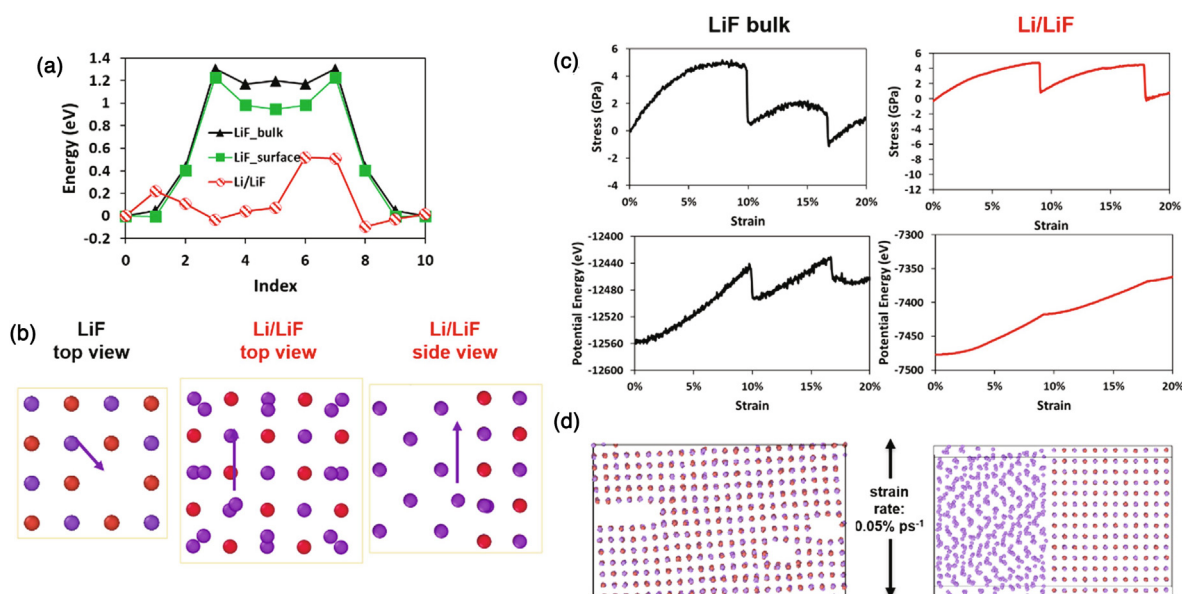


FIGURE 4

(a) MD energy barrier simulation of Li^+ through bulk LiF, the surface of LiF, and along a Li/LiF interface, with (b) LiF crystal and Li/LiF interface pathway schematics. (c) MD stress-strain simulation of (left) LiF crystal and (right) Li/LiF interface, with (top) stress-strain plot, (middle) potential energy-strain plot, and (d) crystal structure at 15% strain. Li and F atoms are shown as purple and red in (b) and (d), respectively.

performances of full cell and will be discussed later. Additionally, the porous structure provides more interfaces between SEI and plated Li, where plating and stripping takes place, thus reducing the local volume fluctuations. Upon the pores being filled, the resultant composite of brittle LiF and ductile Li can further resist SEI cracking. As for the Li/LiF interface in Fig. 4c, there are two sudden drops in stress at 9% and 17.5% strain. However, no obvious sudden drops in the curve of potential energy vs. strain and the well-maintained atomic structure at 15% strain differ from the pure LiF crystal with visible structural fracturing (Fig. 4d). The orientation of LiF and Li is visibly shifted while under 15% strain, which caused the drop in stress. Accordingly, the porous LiF structure, supplying improved Li/LiF interfaces when lithiated, undergoes a reorientation when under strain rather than fracture like pure LiF, therefore lessening the issue of SEI fracture.

Of note, the interconnected pore structure and closed-host design both play an important role and are indispensable. For the closed-host, LiNO_3 stabilizes the in-situ formed SEI through oxidation of sulfur species. This has been confirmed by previous work [3,18], as it has in this work. Electrodes observed post-mortem with XPS revealed a decrease in the amount of polysulfides (Li_2S_x) while increasing the higher oxidation states of sulfur (Li_xSO_y) when LiNO_3 is included (Fig. S8). These polysulfides can play a role even when sulfur cathode is excluded from the cell, where they are obtainable by the decomposition of LiTFSI salt in the electrolyte. The combination of LiTFSI and LiNO_3 salts is necessary to produce an insoluble, electrically insulating SEI with passive Li_xSO_y species, which can minimize further reaction between Li metal and electrolyte [3,18]. This prompts that focus should not only be placed on producing a feasible porous artificial SEI, but also in choosing an optimal electrolyte chemistry to form a stable in-situ SEI layer. In this case, the use of LiNO_3 supported the formation of a stable bi-layer structure, consisting

of a porous LiF-rich inner layer and a dense in-situ formed outer layer.

When there is no LiNO_3 in the electrolyte (i.e., 1 M LiTFSI in 1:1 DOL:DME), an unstable, porous SEI with more polysulfides will be formed (Fig. S8b), which influences the instability of the bi-layer structure, as observed with symmetric cell cycling (Fig. 5a). Regardless of anode treatment (polished Li, dense LiF artificial SEI, porous LiF artificial SEI), the absence of LiNO_3 leads to ultimate failure of symmetric cell via increasing cell resistance, suggesting the formation of dead Li or severe SEI build-up. However, after 150 cycles, the porous LiF symmetric cell exhibits lower voltage hysteresis (200 mV) than the other anode treatments (455 mV for polished Li, 420 mV for dense LiF). Also, consistent with the cycling performances, post-mortem FESEM reveals less mossy Li, as well as less surface fracture over cycling for the porous LiF treatment (Fig. S9). This suggests that the porous structure promotes a more uniform deposition of Li at the early stage of growth, thus lessening internal cell resistance at later cycles comparatively to dense LiF or polished Li. However, the closed-host design is not accomplished when LiNO_3 is removed from the electrolyte, thus allowing consumption of active materials to occur.

The porous LiF anode treatment was further observed with cryo-FIB-SEM after a single 1 mAh/cm² lithiation, where LiNO_3 was included or excluded from the symmetric cell (Fig. 5b-e). Assuming uniform Li^+ flux, the 1 mAh/cm² capacity would result in ~5 μm of plated lithium. The thickness of the porous SEI is nearly 5 μm , which means the growth of metallic lithium will inevitably penetrate the porous layer, plating some under the porous layer. Continuous parasitic reaction will happen if there is no protection of a stable, electrically insulating top SEI layer. The porous LiF electrode without LiNO_3 formed an extremely porous, thick SEI after lithiation, where a large amount of

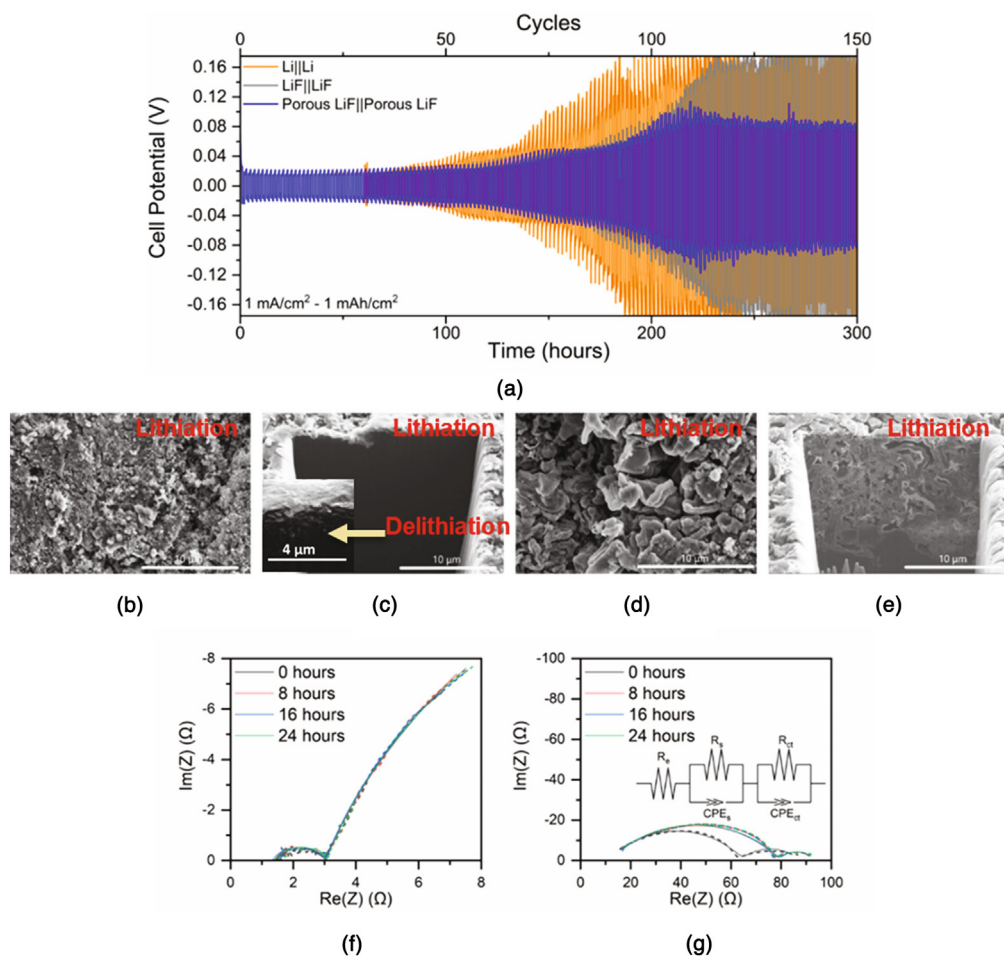


FIGURE 5

(a) Symmetric cell cycling of different anode treatments without LiNO_3 in the electrolyte. (b, d) Surface and (c, e) cross-section cryo-FIB-SEM of porous LiF anode after a single lithiation cycle in a symmetric cell (b, c) with LiNO_3 and (d, e) without LiNO_3 . (f–g) The inset in Figure (c) shows cross-section cryo-FIB-SEM of porous LiF anode after delithiation with LiNO_3 . EIS spectra of porous LiF symmetric cells (f) with LiNO_3 and (g) without LiNO_3 , as a function of time at rest after cycling (>100 cycles), with the equivalent circuit model and fits included (raw data as dashes, equivalent circuit fits as solid lines).

lithium was consumed, which is consistent with the presence of polysulfides confirmed with XPS depth profiling (Fig. S8a and b). When LiNO_3 is included, the resulting SEI after lithiation is incredibly compact (Fig. 5c). The pores of the artificial SEI appear to be filled with plated lithium. After subsequent delithiation, the porous structure is visibly retained (inset of Fig. 5c and Fig. S10a). After further cycling, the in-situ thin SEI layer was observed with the thickness of ranging 100 s of nanometers, which suppresses further Li loss (inset of Fig. 5c and Fig. S10b), agreeing well with the absence of polysulfides beneath the SEI layer (Fig. S8). The stabilization of the bi-layer structure is further supported by collecting EIS spectra as a function of rest without cycling (Fig. S11) when compared to cells with and without LiNO_3 after cycling (Fig. 5f and g). The Nyquist plots presented are fit with an equivalent circuit consisting of SEI resistance (R_s) and charge-transfer resistance (R_{ct}) in parallel with constant phase elements (CPE), as well as electrolyte resistance (R_e) (Fig. 5g, inset) [53–56]. Complete resistance data for equivalent circuit fits is provided in Table S1. In the case of resting without cycling, the bi-layer structure has yet to be realized (i.e., open-host), and therefore the SEI resistance continues to increase over

time. After cycling and the closed host has formed, a low SEI resistance is maintained ($\sim 1.6 \Omega$ at each time interval), while an increase in SEI impedance from 0 to 8 h resting is seen when LiNO_3 is excluded from the electrolyte (52.6 to 67.3 Ω). Additionally, the initial SEI resistance of the symmetric cell without LiNO_3 at 0-hour rest is exceptionally greater than the impedance seen for the cell with LiNO_3 (52.6 Ω versus 1.6 Ω) due to severe electrolyte loss (side reaction) and SEI build-up after 100 cycles. This reveals that the dense in-situ SEI formation fulfills the closed-host design. In summary, such a bi-layer structure will allow uniform Li plating/stripping, suppress Li dendrite growth, and minimize parasitic reaction while also reducing the stress placed on SEI and subsequent fracture that plagues the dense LiF artificial SEI.

In the approach to make the porous layer, tailoring the amount of I_2 (elemental iodine to fluorine, i.e., I:F ratio) in the precursor solution has an effect on cell performance, likely driven by a direct correlation to the porosity or tortuosity of the artificial SEI (Fig. S12). The 1:3 I:F ratio was chosen as the optimized concentration in the precursor, showing the lowest stabilized voltage hysteresis under 30 mV, which ultimately defined the

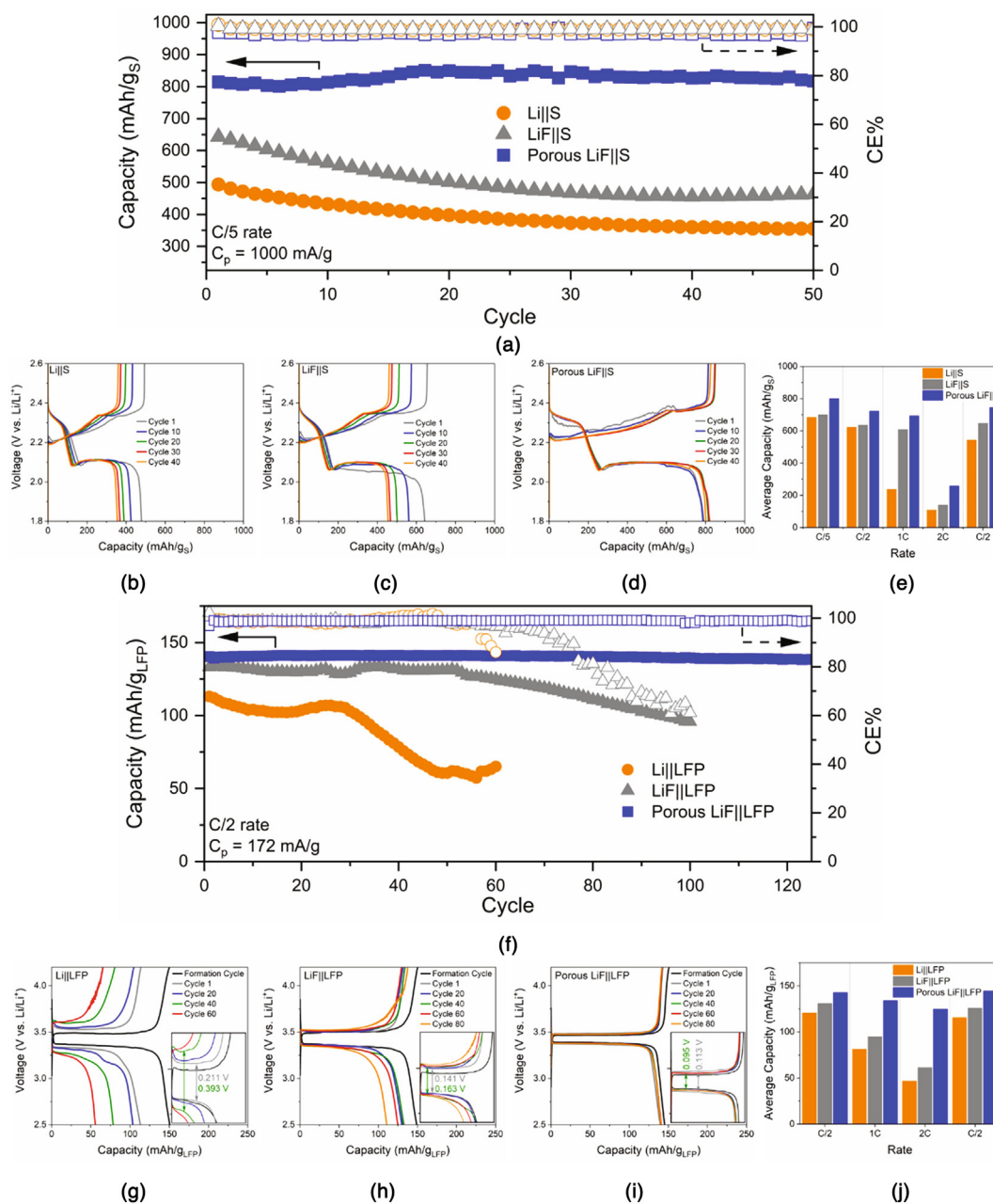


FIGURE 6

(a) Li-S cell galvanostatic cycling at C/5 rate with (b–d) charge–discharge curves for (b) Li, (c) LiF, and (d) porous LiF anode cell, as well as (e) rate performance testing. (f) Li–LFP cell galvanostatic cycling at C/2 rate with (g–i) charge–discharge curves for (g) Li, (h) LiF, and (i) porous LiF anode cell, as well as (j) rate performance testing.

superior SEI porosity or tortuosity to be used in full-cell testing with both sulfur and LiFePO₄ (LFP) cathodes.

The improvement of lithium anode with a bi-layer SEI consisting of porous LiF artificial SEI and dense in-situ SEI is further confirmed with sulfur-based cathode full-cell testing. Cyclic voltammograms maintained similar peak location and intensity with different anode treatments (Fig. S13a) [57]. For cycling performance, initial formation cycles at a C/20 rate support the construction of the bi-layer structure, being used to stabilize the anode. After the formation cycles, the porous LiF outperformed dense LiF and polished Li anodes, shown in Fig. 6a–c. With galvanostatic cycling at a C/5 rate (Fig. 6a), the discharge capacity of

the porous LiF cell was maintained above 820 mAh/g after 50 cycles with little to no capacity fading, while the dense LiF and polished Li cells provided lower capacities of 515 and 355 mAh/g, respectively. Along with lower capacities, the dense LiF and polished Li suffered early cycle capacity fade (Fig. 6b–c). This reveals the enhanced stability of the anode with bi-layer structure that allows increased capacity and capacity retention after 50 cycles. Further evidence of a stable anode is shown with post-mortem FESEM (Fig. S14), where the anode treated with the bi-layer SEI retained a dense SEI with lower sulfur-content when compared to the polished Li and dense LiF anode. The relatively similar surface morphologies of cathodes before and after

cycling also suggests that surface chemistry did not drastically change, thus corresponding to the reduced polysulfide shuttling effect due to stable SEI.

To exclude the shuttling effect on cyclability in Li-S cells, the stable LFP cathode with areal capacity of 2.4 mAh/cm² was also used to further exhibit the feasibility of the novel bi-layer porous/dense SEI. After formation cycles at a C/5 rate, galvanostatic cycling at a C/2 rate revealed extended cycle life due to the construction of the bi-layer SEI structure on the anode surface (Fig. 6f). Following similar initial formation cycle capacities (~145–150 mAh/g, Fig. 6g–i), the initial aging discharge capacity for polished Li was drastically lower than the artificial SEI treatments and faded rapidly after ~30 cycles. The cell with bi-layer SEI maintained a capacity of 138 mAh/g with 98.7% CE% and 99.2% of capacity retention as well as a highly compact and uniform surface (Fig. S15) after 125 cycles. Comparatively, dense LiF had less stable capacity retention, showing fade after ~55 cycles and resulting with a capacity of 95 mAh/g and 60% CE% as well as anode surface fracture (Fig. S15) after 100 cycles. The full cell testing results are in a good agreement with symmetric cell results.

Further, we found the bi-layer SEI design did not sacrifice rate performance. When observing the charge–discharge curves (Fig. 6g–i), the polarization (i.e., difference between charge and discharge voltage plateaus) is lower for porous LiF than polished Li and dense LiF. The rate capacities for Li-S and Li-LFP full cells are summarized in Fig. 6e and j, respectively. Similarly, the cell anode with bi-layer SEI design depicts the highest rate performances. This relates back to the increase in LiF|Li interfaces and the improved Li⁺ conductivity along the LiF|Li interface due to significantly reduced energy barrier for Li⁺ transport (0.6 eV) (Fig. 4a). In addition, the closed-host bi-layer structure can be applied in the high-voltage Li-metal batteries with high Ni-NMC as the cathode. However, the electrolyte, such as carbonate-based electrolyte with FEC as the additive [15,50,58], which can resist high voltage, should be used in place of the one (DOL:DME) used in this work. Alternatively, the relatively dense top SEI layer can be ex-situ formed, which will be studied later. Nevertheless, the current work as the proof-of-concept is sufficient.

Conclusions

We demonstrated a bi-layer structure, constructed of an interconnected, tortuous, porous LiF-rich layer in contact with lithium and a dense in-situ formed inorganic-rich layer on top of the porous structure, showing enhanced anode stability. This was produced through a facile method of forming a composite LiI–LiF coating, followed by dissolving the LiI with a solvent rinse. The resulting artificial SEI was a LiF-rich, porous structure, where an increased number of Li/LiF interfaces for lithium nucleation are made available, thus reducing local volume fluctuations, improving the flexibility of the SEI, as well as decreasing anode resistance due to faster Li⁺ diffusion along such interface. Additionally, the interconnected and tortuous pores improve the Li⁺ flux distribution and mechanically suppresses dendrite growth, which usually occur due to chemical or topographical heterogeneities on the Li-metal surface. In early cycling, lithiated

sites near the electrolyte are consumed to form a dense, electrically insulating upper layer of inorganic-rich SEI, thus realizing the closed-host bi-layered structure. This top layer reduces the side reaction, allowing extended cyclability on the Li-metal side. This was validated with symmetric cell cycling at different rates and areal capacities, as well as with full-cell testing using both sulfur and LFP cathodes. The design of a closed-host bi-layer structure, consisting of an electrically insulating dense top layer and porous bottom layer, opens the new opportunity to improve the stability of the Li-metal anode and unlock a plausible route for high-energy metal-based batteries, such as Li, Na and K metals.

CRedit authorship contribution statement

Corey M. Efav: Conceptualization, Writing - original draft, Visualization, Methodology, Validation, Investigation. **Bingyu Lu:** Methodology, Investigation. **Yuxiao Lin:** Methodology, Writing - original draft. **Gorakh M. Pawar:** Methodology, Writing - original draft. **Parameswara R. Chinnam:** Investigation. **Michael F. Hurley:** Supervision, Funding acquisition. **Eric J. Dufek:** Writing - review & editing, Supervision, Funding acquisition. **Ying Shirley Meng:** Writing - review & editing, Supervision, Funding acquisition. **Bin Li:** Conceptualization, Writing - original draft, Writing - review & editing, Supervision, Funding acquisition.

Declaration of Competing Interest

The authors declare that they have no known competing financial interests or personal relationships that could have appeared to influence the work reported in this paper.

Acknowledgements

Research has been supported by the Assistant Secretary for Energy Efficiency and Renewable Energy, Office of Vehicle Technologies of the U.S. Department of Energy through the Advanced Battery Materials Research Program (Battery500 Consortium). INL is operated by Battelle Energy Alliance under Contract Nos. DE-AC07-05ID14517 for the U.S. Department of Energy. The U.S. Government retains and the publisher, by accepting the article for publication, acknowledges that the United States Government retains a nonexclusive, paid-up, irrevocable, world-wide license to publish or reproduce the published form of this manuscript, or allow others to do so, for U.S. Government purposes. The glovebox AFM used in this work was funded through the National Science Foundation Grant No. 1727026 and accessed through the Boise State Surface Science Laboratory. The authors acknowledge the Atomic Films Laboratory at Boise State University for the use of the PHI-5600 XPS system. The authors would like to thank JD Hues, Nicholas Bulloss, and Paul H. Davis of Boise State University for support with XPS, FESEM, and AFM, respectively, and thank Charles C. Dickerson, Yulun Zhang, and Ningshengjie Gao of Idaho National Laboratory for help with electrochemical testing.

Appendix A. Supplementary data

Supplementary data to this article can be found online at <https://doi.org/10.1016/j.mattod.2021.04.018>.

References

- [1] Z.W. Seh et al., *Chem. Soc. Rev.* 45 (20) (2016) 5605–5634, <https://doi.org/10.1039/C5CS00410A>.
- [2] P.G. Bruce, L.J. Hardwick, K.M. Abraham, *MRS Bull.* 36 (7) (2011) 506–512, <https://doi.org/10.1557/mrs.2011.157>.
- [3] D. Aurbach et al., *J. Electrochem. Soc.* 156 (8) (2009) A694–A702, <https://doi.org/10.1149/1.3148721>.
- [4] X.S. Xiong et al., *Front. Chem.* 7 (2019), <https://doi.org/10.3389/fchem.2019.00827>.
- [5] W. Xu et al., *Environ Sci* 7 (2) (2014) 513–537, <https://doi.org/10.1039/c3ee40795k>.
- [6] D.C. Lin, Y.Y. Liu, Y. Cui, *Nat. Nanotechnol.* 12 (3) (2017) 194–206, <https://doi.org/10.1038/Nnano.2017.16>.
- [7] X.B. Cheng et al., *Chem. Rev.* 117 (15) (2017) 10403–10473, <https://doi.org/10.1021/acs.chemrev.7b00115>.
- [8] J. Liu et al., *Energy* 4 (3) (2019) 180–186, <https://doi.org/10.1038/s41560-019-0338-x>.
- [9] G. Wang et al., *Energy Storage Mater.* 23 (2019) 701–706, <https://doi.org/10.1016/j.ensm.2019.02.026>.
- [10] X.B. Cheng et al., *Adv. Mater.* 28 (15) (2016) 2888–2895, <https://doi.org/10.1002/adma.201506124>.
- [11] L. Enze, *J. Phys. D Appl. Phys.* 20 (12) (1987) 1609–1615, <https://doi.org/10.1088/0022-3727/20/12/011>.
- [12] H.L. Dai et al., *Nat. Commun.* 11 (1) (2020), <https://doi.org/10.1038/s41467-020-14505-8>.
- [13] Z.A. Yu et al., *Joule* 3 (11) (2019) 2761–2776, <https://doi.org/10.1016/j.joule.2019.07.025>.
- [14] J.L. Lang et al., *Energy Storage Mater.* 16 (2019) 85–90, <https://doi.org/10.1016/j.ensm.2018.04.024>.
- [15] D. Lin et al., *Nano Lett.* 17 (6) (2017) 3731–3737, <https://doi.org/10.1021/acs.nanolett.7b01020>.
- [16] Y.Z. Li et al., *Joule* 2 (10) (2018) 2167–2177, <https://doi.org/10.1016/j.joule.2018.08.004>.
- [17] E. Peled, S. Menkin, *J. Electrochem. Soc.* 164 (7) (2017) A1703–A1719, <https://doi.org/10.1149/2.1441707jes>.
- [18] S.Z. Xiong et al., *J. Power Sources* 246 (2014) 840–845, <https://doi.org/10.1016/j.jpowsour.2013.08.041>.
- [19] C.X. Xu, J.J. Jiang, *Rare Metals* 40 (2) (2021) 243–245, <https://doi.org/10.1007/s12598-020-01629-5>.
- [20] S. Chen et al., *Adv. Mater.* 30 (21) (2018) 1706102, <https://doi.org/10.1002/adma.201706102>.
- [21] S.R. Chen et al., *Joule* 2 (8) (2018) 1548–1558, <https://doi.org/10.1016/j.joule.2018.05.002>.
- [22] X.D. Ren et al., *Joule* 3 (7) (2019) 1662–1676, <https://doi.org/10.1016/j.joule.2019.05.006>.
- [23] S.M. Wood et al., *Adv. Energy Mater.* 8 (26) (2018), <https://doi.org/10.1002/aenm.201801427>.
- [24] L. Chen et al., *ACS Appl. Mater. Interfaces* 10 (32) (2018) 26972–26981, <https://doi.org/10.1021/acsami.8b04573>.
- [25] J. Ko, Y.S. Yoon, *Ceram. Int.* 45 (1) (2019) 30–49, <https://doi.org/10.1016/j.ceramint.2018.09.287>.
- [26] M.F. He et al., *Proc. Natl. Acad. Sci. U.S.A.* 117 (1) (2020) 73–79, <https://doi.org/10.1073/pnas.1911017116>.
- [27] Y.X. Yuan et al., *J. Energy Chem.* 37 (2019) 197–203, <https://doi.org/10.1016/j.jechem.2019.03.014>.
- [28] H. Zhang et al., *Nat. Commun* 9 (1) (2018), <https://doi.org/10.1038/s41467-018-06126-z>.
- [29] Y. Liu et al., *ACS Nano* 11 (8) (2017) 8519–8526, <https://doi.org/10.1021/acsnano.7b04617>.
- [30] K.-H. Chen et al., *J. Power Sources* 471 (2020) 228475, <https://doi.org/10.1016/j.jpowsour.2020.228475>.
- [31] C. Yan et al., *Adv. Mater.* 30 (45) (2018), <https://doi.org/10.1002/adma.201804461>.
- [32] M.K. Datta et al., *J. Power Sources* 467 (2020), <https://doi.org/10.1016/j.jpowsour.2020.228243>.
- [33] C. Wang et al., *Adv. Funct. Mater.* 29 (49) (2019), <https://doi.org/10.1002/adfm.201905940>.
- [34] C.M. Efav et al., *J. Electrochem. Soc.* 166 (11) (2019) C3018–C3027, <https://doi.org/10.1149/2.0041911jes>.
- [35] S. Plimpton, *J. Comput. Phys.* 117 (1) (1995) 1–19, <https://doi.org/10.1006/jcph.1995.1039>.
- [36] A. Stukowski, *Model. Simul. Mater. Sci.* 18 (1) (2010), <https://doi.org/10.1088/0965-0393/18/1/015012>.
- [37] I. Medea version 3.1; Medea is a registered trademark of Materials Design, San Diego, USA.
- [38] Z.W. Cui et al., *J. Power Sources* 207 (2012) 150–159, <https://doi.org/10.1016/j.jpowsour.2012.01.145>.
- [39] X. Wang et al., *Nat. Mater.* 19 (12) (2020) 1339–1345.
- [40] X.W. Zhou, F.P. Doty, *Phys. Rev. B* 78 (22) (2008), <https://doi.org/10.1103/PhysRevB.78.224307>.
- [41] A.K. Rappe, et al. *J. Am. Chem. Soc.* 114 (25); (1992): 10024–10035. <https://doi.org/10.1021/ja00051a040>.
- [42] Z. Liu et al., *J. Electrochem. Soc.* 163 (3) (2016) A592–A598, <https://doi.org/10.1149/2.0151605jes>.
- [43] L. Benitez, J.M. Seminario, *J. Electrochem. Soc.* 164 (11); (2017): E3159–E3170. <https://doi.org/10.1149/2.0181711jes>.
- [44] T. Ao et al., *J. Appl. Phys.* 106 (10) (2009) 103507, <https://doi.org/10.1063/1.3259387>.
- [45] X. Ji et al., *Adv. Mater.* 32 (46) (2020), <https://doi.org/10.1002/adma.202002741>.
- [46] A. Huang et al., *Adv. Mater.* 32 (14) (2020), <https://doi.org/10.1002/adma.201907516>.
- [47] R. Mogi et al., *J. Electrochem. Soc.* 149 (12) (2002) A1578–A1583, <https://doi.org/10.1149/1.1516770>.
- [48] C. Shen et al., *Methods* 2 (2) (2018), <https://doi.org/10.1002/smt.201700298>.
- [49] C. Shen et al., *ACS Appl. Mater. Interfaces* 7 (45) (2015) 25441–25447, <https://doi.org/10.1021/acsami.5b08238>.
- [50] X.-Q. Zhang et al., *Adv. Funct. Mater.* 27 (10) (2017), <https://doi.org/10.1002/adfm.201605989>.
- [51] B.B. Wu et al., *Nano Energy* 40 (2017) 34–41, <https://doi.org/10.1016/j.nanoen.2017.08.005>.
- [52] J. Chen et al., *Energy* 5 (5) (2020) 386–397, <https://doi.org/10.1038/s41560-020-0601-1>.
- [53] D. Aurbach et al., *J. Power Sources* 81 (1999) 95–111, [https://doi.org/10.1016/S0378-7753\(99\)00187-1](https://doi.org/10.1016/S0378-7753(99)00187-1).
- [54] E. Kazyak, K.N. Wood, N.P. Dasgupta, *Chem. Mater.* 27 (18) (2015) 6457–6462, <https://doi.org/10.1021/acs.chemmater.5b02789>.
- [55] L.P. Wang et al., *J. Power Sources* 342 (2017) 175–182, <https://doi.org/10.1016/j.jpowsour.2016.11.097>.
- [56] G. Bieker, M. Winter, P. Bieker, *Phys. Chem. Chem. Phys.* 17 (14) (2015) 8670–8679, <https://doi.org/10.1039/c4cp05865h>.
- [57] Y. Zhang, *ACS Appl. Energy Mater.* 3 (5) (2020) 4173–4179, <https://doi.org/10.1021/acsaem.0c00568>.
- [58] E. Markevich et al., *ACS Energy Lett.* 2 (6) (2017) 1321–1326, <https://doi.org/10.1021/acsenerylett.7b00300>.